Extremely large water droplet impact onto a deep liquid pool

Sandip Dighe,[1,*] Dilip Kumar Maity,[1] Jeffrey N. Fonnesbeck,[1] Som Dutta,[2] and Tadd Truscott[1,†]

[1]*Mechanical Engineering Program, Physical Science and Engineering Division, King Abdullah University of Science and Technology, Thuwal 23955, Kingdom of Saudi Arabia*

[2]*Department of Mechanical Engineering, Utah State University, Logan, Utah 84322, USA*

(Received 16 February 2023; revised 6 November 2023; accepted 19 February 2024; published 16 April 2024)

Most studies of droplet impact on liquid pools focus on droplet diameters up to the capillary length (0.27 cm). We break from convention and study extremely large water droplets (1 to 6 cm diameter) falling into a pool of water. We demonstrate that the depth and width of the cavity formed by large droplet impact is greatly influenced by the deformed shape of the droplet at impact (i.e., prolate, spherical, and oblate), and larger droplets amplify this behavior by flattening before impact. In particular, the maximum cavity depth is a function of the Froude number and axis ratio of the droplet just before impact. Further, the cavity depth is more dependent on the droplet height than width, and the maximum cavity diameter is independent of the droplet height. In general, we observe that more oblate droplets result in decreasing cavity depths for a fixed liquid volume. This is because an increase in horizontal droplet diameter results in a reduced impact energy flux and therefore reduced cavity depth.

DOI: 10.1103/PhysRevE.109.045107

I. INTRODUCTION

A liquid droplet falling onto a deep liquid pool [Fig. 1(a), $t = -1.14$ ms] leads to the formation of a thin liquid sheet above the liquid surface known as a splash crown and a subsurface cavity ($t = 15.4$ ms). As the cavity retracts a liquid jet is formed ($t = 178$ ms), also known as a Worthington jet [2,3]. Droplet diameters smaller than the capillary length ($\lambda = 0.27$ cm) where surface tension dominates gravitational forces that fall into a deep pool of water tend to form hemispherical subsurface cavities [4–8]. These smaller droplets are assumed to be spherical, yet all droplets oscillate after release in a fundamental mode as predicted by Rayleigh, whether they are released by a needle or naturally disturbed by drag forces [9–12]. Although small droplets have correspondingly small axis ratios [b/a, b and a are the maximum vertical and horizontal droplet dimensions respectively; see Fig. 1(b)], the literature suggests that some impact cases can form cavities deeper than the theoretical maximum (e.g., when $b/a > 1$). Although evident in the literature, the reasoning behind the discrepancy remains unstudied as most models assume spherical droplets [4–7].

In this article, we show that droplet axis ratio variation plays a large role in the depth of penetration, where prolate droplets ($b/a > 1$) penetrate deeper than oblate ones ($b/a < 1$). Axis ratios become larger and affect cavity formation more if the droplet diameter (d_0) is larger than λ. The droplet size sets terminal velocity in free fall and b/a becomes significant when a water droplet diameter in air is $d_0 > 4.3$ mm [13,14] (i.e., Weber number $\mathrm{We} = \rho V^2 d_0/\sigma > 6.54$, ρ is air density, V is velocity, and d_0 is the spherical droplet diameter). These oscillations lead to the breakup of the droplet if $b/a \gtrsim \pi$ [13]. As droplets get larger they tend to flatten and break up because of drag rather than oscillations when $\mathrm{We} > 13$ (e.g., $d_0 > 6.1$ mm for water) [14–24,46]. This is in fact the main reason why forming a water droplet much larger than 2λ is so difficult and ignored by most studies [34–45].

It is commonly held that the normalized maximum cavity depth ($h_{\max}/d_0$) of a small droplet is a function of the droplet impact Froude number $(\mathrm{Fr})^{1/4}$ [4] where $\mathrm{Fr} = V^2/gd_0$. However, our study shows that this relationship is not generalized enough for deformed droplets and deformed cavities. The normalized maximum cavity depth ($h_{\max}/d_0$) can be scaled properly by the Froude number and the axis ratio $[\mathrm{Fr}(b/a)]^{1/4}$, including small droplets, and $h_{\max}$ is more strongly dependent on b than a. Further, we show that the cavity width (D_h) at the time of maximum cavity depth is independent of droplet height (b). This means that the cavity shape of a large droplet impact is not necessarily hemispherical as commonly observed for smaller droplets ($d_0 \leqslant \lambda$).

The contribution here is twofold: (1) oblate and prolate extremes, which all droplets have by the nature of the Rayleigh condition [13], can alter cavity formation (see Fig. 1), and (2) droplets larger than the capillary length tend to make shallower cavities as they flatten, which they inevitably do as they increase their speed. The relevance to the physical world is that in large-splash small-velocity applications (i.e., wave crashing) large droplets are formed and their behavior after impact is not the same as a single small droplet impact. Small droplets are dominated by surface tension while large droplets

*sandiplaxmandighe@gmail.com
†taddtruscott@gmail.com

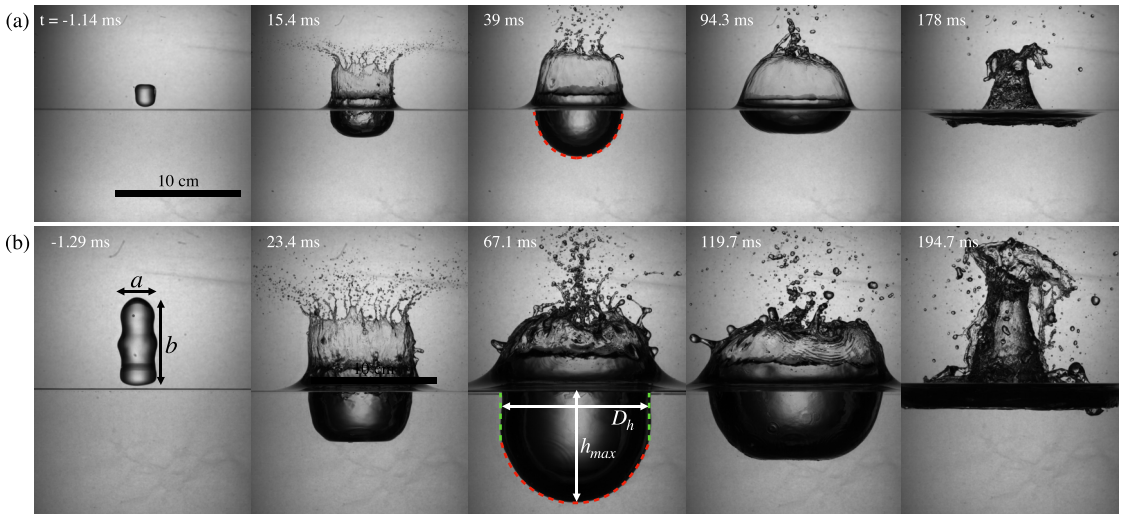

FIG. 1. Sequence of the extremely large droplet impact onto a deep liquid pool showing the difference in the cavity formed by a nearly spherical ($b/a \sim 1$) and a prolate ($b/a > 1$) droplet. Nearly spherical droplet, $\mathcal{V}_d = 4.200$ ml, $d_0 = 2.00$ cm, and H (release height) $= 95$ cm (a). Prolate droplet, $\mathcal{V}_d = 37.0$ ml, $d_0 = 4.14$ cm, and $H = 95$ cm (b). The width a and height b of the droplet just before impact are marked in (b) at $t = -1.29$ ms, and similar measurements are made for each case. The red dotted line outlines the two different cavity shapes at the event of the maximum cavity depth (i.e., definition of $h_{\max}$ and D_h). For the corresponding videos, see videos 1 & 2 in the Supplemental Material [1].

are dominated by inertia. The findings are important for applications where inertia dominates, ranging from primary wave breakup over the ocean surface [25–27], dampening of the sea wave motion [28,29], oil spills over the ocean surface [30], and planetary impacts [31].

II. EXPERIMENTAL METHOD

The schematic of the experimental setup is provided in Fig. 4 in Appendix A. Large water droplets are released onto a water pool having a 40 cm $\times$ 40 cm cross section with a water depth of 40 cm. Large droplets are made by a droplet maker that minimizes the amplitude of oscillation at release [12]. The droplet maker consists of an arm hinged at one end and connected to a solenoid release at the other end (Fig. 4 in Appendix A), allowing the arm to fall freely when released. The center of mass of the arm is closer to the hinge, which allows the rotational acceleration to be larger than g at the droplet basket end. Various curved mesh surfaces coated with a hydrophobic spray are used to hold the desired amount of the liquid and clamped to the release end of the droplet generator (Fig. 5 in Appendix A). Due to the slight difference in the acceleration between the surface and the droplet, the droplet smoothly separates from the release surface. The details of the droplet volumes used, droplet equivalent diameters, Froude number, and surfaces used for releasing the droplets are provided in Table I in Appendix A. The droplet release height (H) is varied from 65 cm to 215 cm to cover a range of We from 2 to 40 and Fr from 20 to 385. The droplet shapes just before impact and the underwater cavity shapes formed after impact are visualized by a high-speed shadowgraphy technique.

III. RESULTS

Droplets on the order of the capillary length and smaller form hemispherical cavities similar to the time series in Fig. 1(a) and scale with $\mathrm{Fr}^{1/4}$ [4,6,7]. Figure 1 shows the evolution of two cavities after the impact of (a) a 2.00 cm nearly spherical droplet and (b) a 4.14 cm prolate droplet both released from a height of 95 cm. The droplet forms a splash crown and cavity. The cavity reaches a maximum depth of penetration ($h_{\max}$) and then retracts. The evolution of the nondimensional cavity depth with the nondimensional time $t^* = Vt/d_0$ is shown in Fig. 2(a). As Fr increases the cavity retraction time increases, but the maximum cavity depth decreases, because the axis ratio changes from prolate to spherical to oblate as release height is increased. The shape of the droplets just before impact is shown in the inset of Fig. 2(a). Therefore, the cause of the reduction in the cavity depth with an increase in Fr is the shape of the droplet at impact. The variation in the maximum cavity depth with the Froude number is shown in Fig. 2(b). This implies that a more oblate shape decreases the energy flux into the fluid medium for a given droplet volume. For comparison, the theoretical prediction from Pumphrey and Elmore [4] and least-square fit from the work of Leng [6] are also shown. For extremely large droplets (> 3 cm), as the droplet shapes change from prolate to oblate, the maximum cavity depth decreases and the most oblate cases fall outside the prediction (blue markers). For extremely prolate droplets, the maximum cavity depths are larger than the theoretical prediction as indicated by the red markers. Thus, in the case of extremely large droplet impacts, the maximum cavity depth is not merely a function of the Froude number, but also dependent on the droplet axis ratio (b/a).

We observe droplets that can be approximated into three fundamental shapes: prolate, spherical, and oblate [see Figs. 6(a)–6(f) in Appendix A]. Extremely large droplets ($d_0 > 3$ cm) can be deformed to such an extent that they show the classical bag breakup regime [15] [e.g., see Fig. 6(c), case $d_0 = 3.06$ cm and Fr ~ 141]. It is well known that the

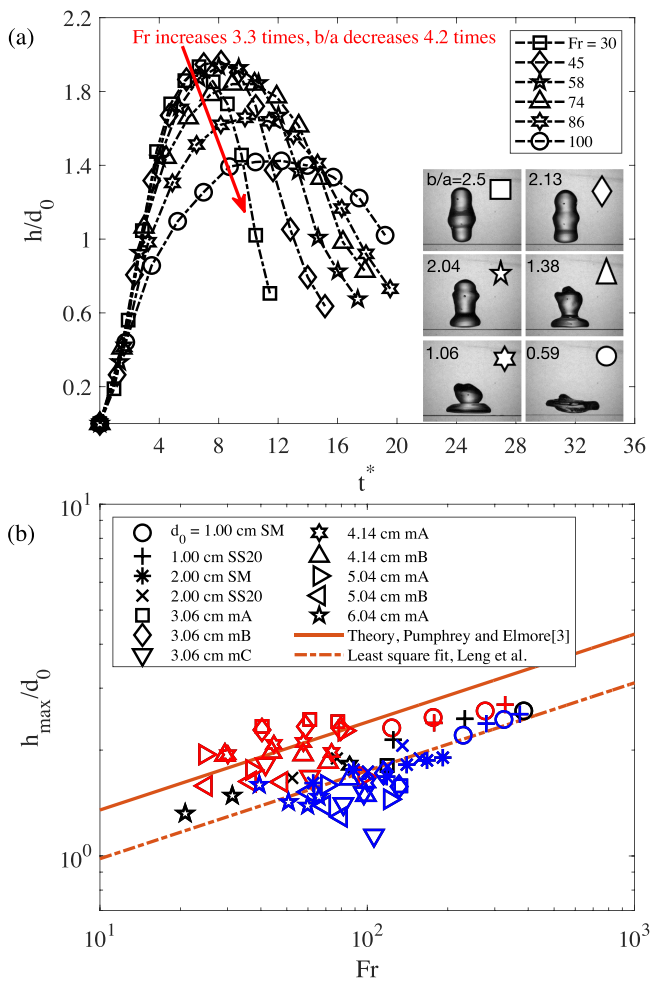

FIG. 2. (a) Evolution of the cavity depth versus non-dimensional time for increasing Froude numbers, $d_0 = 4.14$ cm. (b) Dimensionless maximum cavity depth vs Froude number is compared against the theoretical curve given by Pumphrey and Elmore [4] ($h_{\max}/d_0 = (Fr/3)^{1/4}$) and least-square fit [$h_{\max}/d_0 = 0.727(Fr/3)^{1/4}$] to the experimental data for small droplets given by Leng [6]. The red, black, and blue colored markers in (b) show data points for prolate ($b/a > 1.1$), spherical ($0.9 \leqslant b/a \leqslant 1.1$), and oblate ($b/a < 0.9$). The release geometry and mesh type are abbreviated as mesh A (mA), mesh B (mB), Mesh C (mC), sink mesh (SM), and SS20 with more details presented in Fig. 5 in Appendix A.

droplets after release oscillate with a Rayleigh frequency [9]. We confirm that large droplets also oscillate with a frequency predicted by the Rayleigh formula [Eq. (B1) in Appendix B], however, extremely large droplets ($d_0 > 3$ cm) show flattening behavior after one or two oscillations, resulting in the droplet axis ratio increasing with an increase in velocity. Large droplets tend to oscillate between prolate and oblate until they reach a velocity where drag dominates, then they flatten [as shown in Figs. 6(g) and 6(h) in Appendix A]. Although droplets smaller than 2 cm appear to oscillate, once their velocities increase above a critical Weber number ($\mathrm{We}_{cr} \sim 13$) they will also flatten and eventually break up.

Droplet shape differences affect cavity shapes as illustrated in the images of Figs. 3(a)–3(d). Prolate droplets ($b/a > 1$) make deeper narrow cavities, while oblate droplets ($b/a < 1$) make wider, more shallow shapes. The extreme case of a bagging droplet forms a ring cavity with a jet forming in the center before cavity retraction. This behavior is interesting and deserves further study but is out of the context of the current work. The effect of the droplet shape on the cavity aspect ratio for different droplet sizes is shown in Fig. 3(e). Bisighini *et al.* [7] assumed that capillary droplets were spherical ($b/a \approx 1$) and produced hemispherical cavities with aspect ratios from 0.6 to 0.7, which also works well for large droplets in this study when $b/a = 1$. The impact energy flux for a prolate droplet is larger than the oblate droplets, which leads to deeper penetration. A theoretical scaling based on the energy predicts that the cavity aspect ratio ($h_{\max}/D_h$) is a function of droplet axis ratio (b/a) and is well fitted by the square root fitting law as shown in Fig. 3(e). Note that the droplet shapes for $b/a < 1$ are not perfectly oblate, which increases the scatter in the data; indeed, for a few cases droplets deform to a disklike shape due to aerodynamic drag (see Fig. 6).

Pumphrey and Elmore [4] showed that the maximum cavity depth for small, spherical droplet impacts can be obtained by comparing the impact energy of the impacting droplet with the maximum potential energy of the cavity. They assumed the droplet shape was spherical and the cavity hemispherical. Following the same derivation we can write an energy balance assuming the droplet shapes are ellipsoidal and the corresponding cavity shapes as half ellipsoidal. We justify an ellipsoid despite the nonuniformity of the droplets in a comparison with a numerical estimate in Appendix C and highlight the same physically by showing two very different shapes in the inset of Fig. 3(e). Therefore, the kinetic energy (E_{kin}) of the impacting droplet and the maximum potential energy (V_{pot}) of the cavity formed can be expressed as (a detailed derivation is provided in Appendix C)

$$E_{\mathrm{kin}} = \frac{\rho\pi a^2 b V^2}{12}, \tag{1}$$

$$V_{\mathrm{pot}} = \frac{g\rho\pi h_{\max}^2 D_h^2}{16}. \tag{2}$$

Comparing the kinetic energy of the droplet and the maximum potential energy of the cavity and including an energy conversion factor (K^4) yields

$$\frac{h_{\max} D_h}{2ab} = K^2 \left(\frac{V^2}{3gb}\right)^{1/2}. \tag{3}$$

Our first assumption is based on the work of Leng [6], who showed that about 28% of the kinetic energy is converted into the cavity potential energy for spherical droplet impacts. In the present study, we test this energy argument by considering the energy conversion factor $K = (\frac{V_{\mathrm{pot}}}{E_{\mathrm{kin}}})^{1/4}$ and find that $K = 0.72$ obtained by the ellipsoidal assumption. Equation (3) can then be written as

$$\frac{h_{\max} d_h}{2ab} = 0.72^2 \left(\frac{V^2}{3gb}\right)^{1/2}. \tag{4}$$

Simplifying Eq. (4) we get

$$\frac{h_{\max}}{D_h} = 0.72^2 \sqrt{\frac{4V^2 a^3}{3gD_h^4}} \sqrt{\frac{b}{a}}. \tag{5}$$

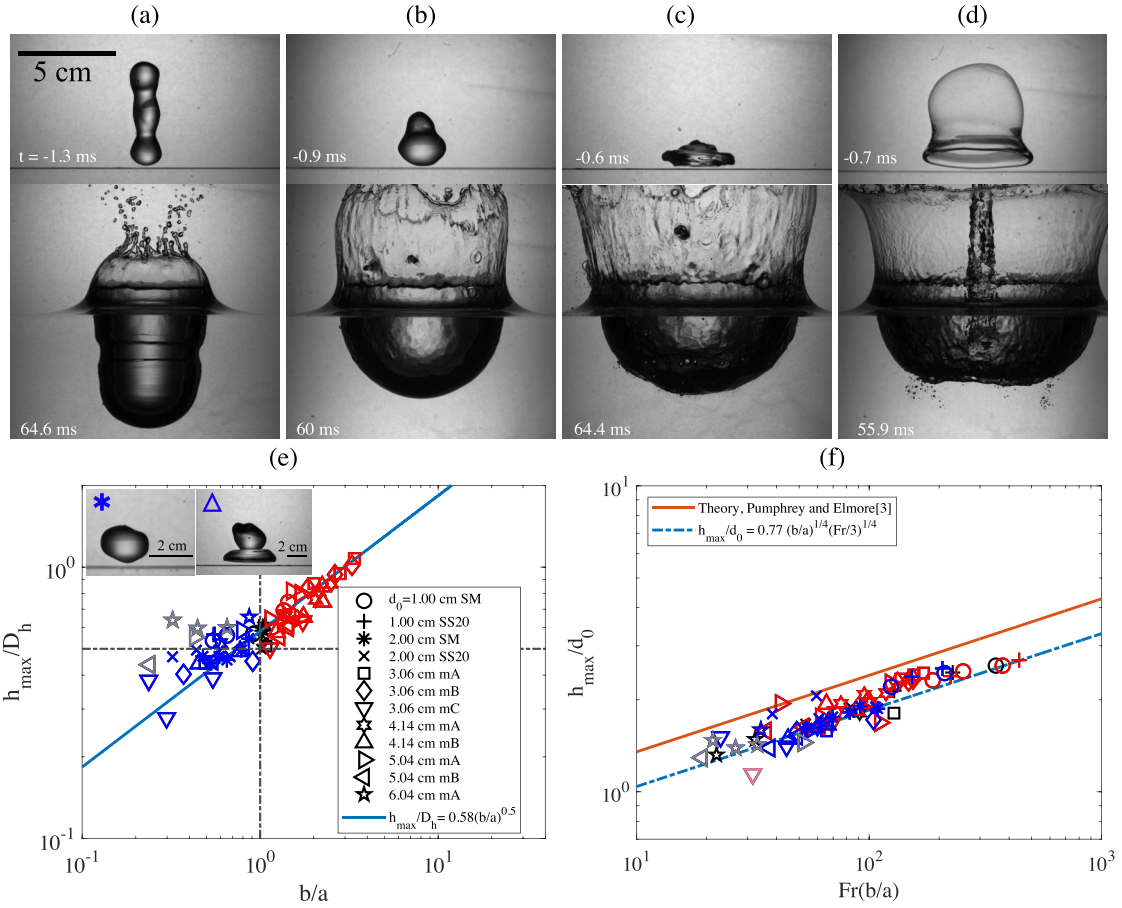

FIG. 3. For a fixed volume ($V_d = 15.0$ ml), three distinct droplet shapes along with the bagging regime at impact and the corresponding cavity shapes at the event of the maximum cavity depth, (a) prolate $H = 65$ cm, (b) nearly spherical $H = 95$ cm, (c) oblate $H = 185$ cm, and (d) bag, $H = 215$ cm. For the corresponding videos see videos 3–6 in the Supplemental Material [1]. Time is shown with reference to the impact event, and the scale shown in (a) is the same for all the images. (e) Variation of the cavity aspect ratio with the droplet axis ratio. Inset highlights two similar b/a ratios but different droplet shapes: (left) $b/a = 0.79$, $h_{max}/D_h = 0.49$, and (right) $b/a = 0.77$, $h_{max}/D_h = 0.48$. (f) Maximum cavity depth as a function of Froude number and droplet axis ratio [scaling relation Eq. (8)]. The red, black, and blue colored markers in (e) and (f) show data points for $b/a > 1.1$, $0.9 < b/a < 1.1$, and $b/a < 0.9$, respectively. A few data points colored in gray in (e) and (f) do not obey the relationship in Eq. (6) (see Appendix C for more information). The light red inverted triangle in (f) corresponds to the "inner empty volume" droplet shape.

In the present study, the experimental data show that the value of the term

$$\sqrt{4V^2a^3/3gD_h^4} = c \tag{6}$$

can be approximated by a constant [see Fig. 10(a) in Appendix C]. Thus, we can make a second assumption that D_h depends on a and is independent of b [Fig. 10(b)]. The mean value of $c = 1.12$, and using this value, the combined constants in Eq. (5) become 0.58. Hence, Eq. (5) can be rewritten as

$$\frac{h_{\max}}{D_h} = 0.58\sqrt{\frac{b}{a}}. \tag{7}$$

Figure 3(e) shows Eq. (7) as a blue line, and it is in good agreement with the experimental data. By combining Eqs. (7) and (6), and conservation of volume (i.e., $a^2b = d_0^3$), we can derive the following scaling relationship:

$$\left(\frac{h_{\max}}{d_0}\right)^4 = 0.77\mathrm{Fr}\frac{b}{a}. \tag{8}$$

Equation (8) describes a key experimental result of this study in terms of the Fr and predicts that the depth of the cavity increases as the axis ratio b/a increases as shown in Fig. 3(f). For nonspherical droplets, this scaling justifies and explains the penetration of the cavity is a function of both Fr and b/a. It captures all of the oblate and prolate data and predicts penetration with much better accuracy using an ellipsoidal assumption even for large droplets. Further, it reveals that $h_{\max}$ depends more strongly on b than on a when we manipulate the result to get $h_{\max}^4 = 0.12\frac{ab^2V^2}{g}$. This is a direct counterpart to the fact that the cavity diameter is influenced only by a [Eq. (6) and Fig. 10(b)]. We can observe this most notably in the impact of a prolate droplet (see video 3 in [1]) where $h_{\max}$ is strongly dependent on b. In the video, the

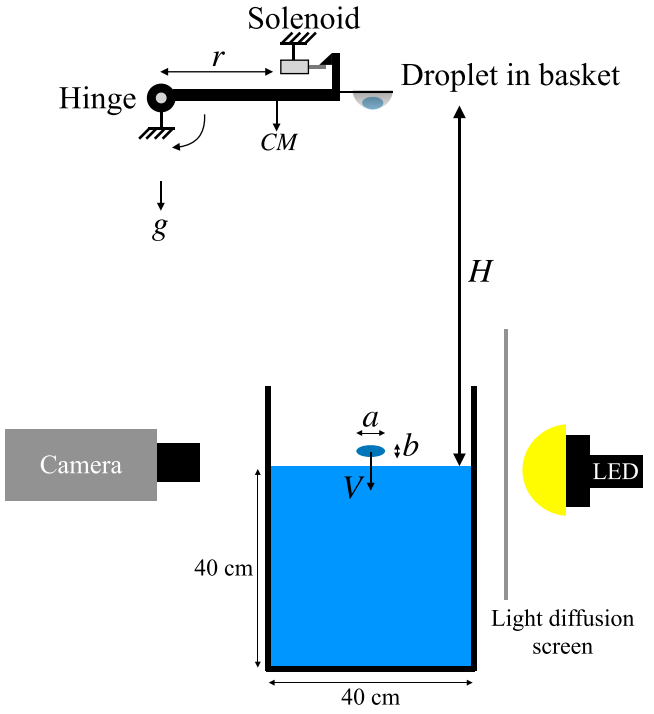

FIG. 4. Schematic of the experimental setup. A droplet release mechanism holds a basket filled with a droplet volume. The solenoid releases the mechanism which is connected to a hinge. The hinge allows the mechanism to rotate. The droplet falls slower than the rotation rate at the basket, thus separating the droplet from the basket. The droplet falls to the surface of the water and impacts with an aspect ratio b/a with velocity V. Images are taken above and below the surface with a camera and an LED providing backlighting.

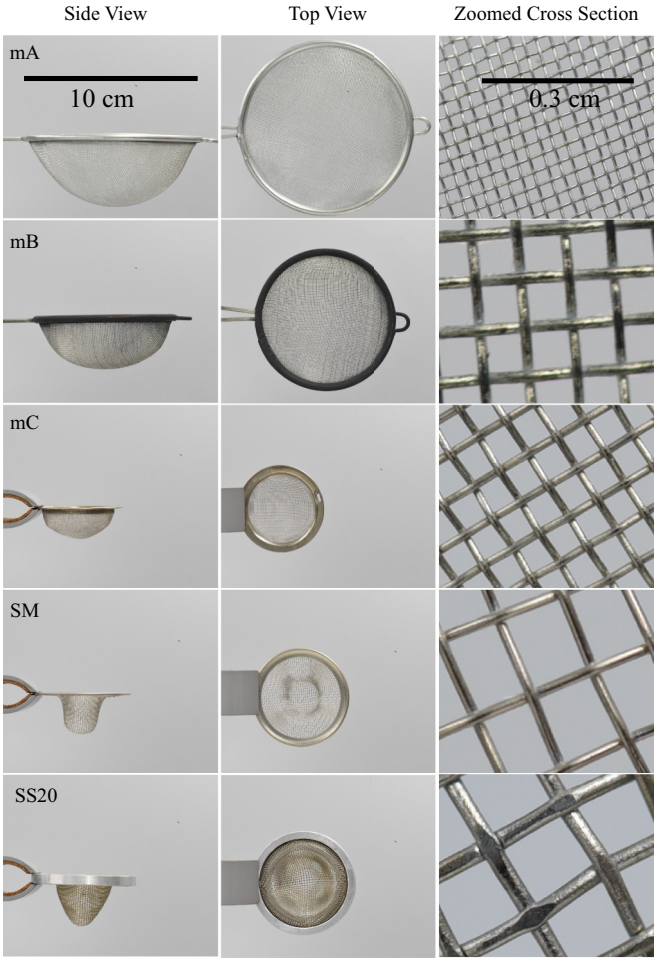

FIG. 5. Release geometries used in the present study. The left column shows the side view, and the middle column shows the top view of the mesh. The scale shown at the top is the same for all the images in the left and middle columns. The right column shows zoomed views of all the meshes, and the scale for images in the right column is shown at the top.

top part of the drop impacts the bottom of an already-formed cavity, resulting in an even deeper cavity being formed (i.e., $h_{\max}$). However, the impact of the top of the droplet on the bottom of the cavity does not widen the cavity at the free surface (i.e., D_h).

IV. CONCLUSION

In conclusion, the cavity shape of a water droplet-pool impact is dependent on the shape of the droplet just before impact. Here we focus on droplet diameters far beyond the capillary length (up to 6 cm), which reveals that cavity depth ($h_{\max}$) is strongly dependent on the height of the droplet (b) and cavity width at the free surface (D_h) is dependent only on the droplet width (a). It is known that even small droplets oscillate as they fall [11,13]. We show that intermediate droplets also oscillate and that the largest droplets we tested tend to flatten as they fall. These extreme shapes allow us to formulate a modified scaling based on potential and kinetic energy similar to the past [4] but with droplet shape taken into account and provide evidence that assuming the droplet is an ellipse is a reasonable assumption. The experimental videos show that prolate droplets form narrow and deep cavities, while oblate droplets form wide and shallow cavities. The depth of the cavity is a function of the Froude number as well as the droplet axis ratio and increases as the droplet axis ratio is increased. The result is a unified scaling for droplet-pool impact from small to very large droplets, allowing future researchers and engineers to predict the cavity behavior of any size and/or shape droplet.

ACKNOWLEDGMENTS

We wish to thank Prof. S. Thoroddsen and his laboratory for helping us set up our laboratory and letting us use their equipment in the interim. Special thanks to K. R. Dharmarajan, F. Kamoliddino, M. Shi, and A. A. Aguirre-Pablo. We would like to thank all our group members for their comments, discussions, and support during this work. Special thanks to A. Katoch, A. Kumar Kushwaha, K. Alhamdan, and S. Truman. We also wish to thank the thorough and thoughtful reviews from the referees.

APPENDIX A: EXPERIMENTAL SETUP

A schematic of the experimental setup is shown in Fig. 4. A 64 watt LED light was used as a backlight. Images were recorded at 7000 frames/sec having 1024×1024 pixels

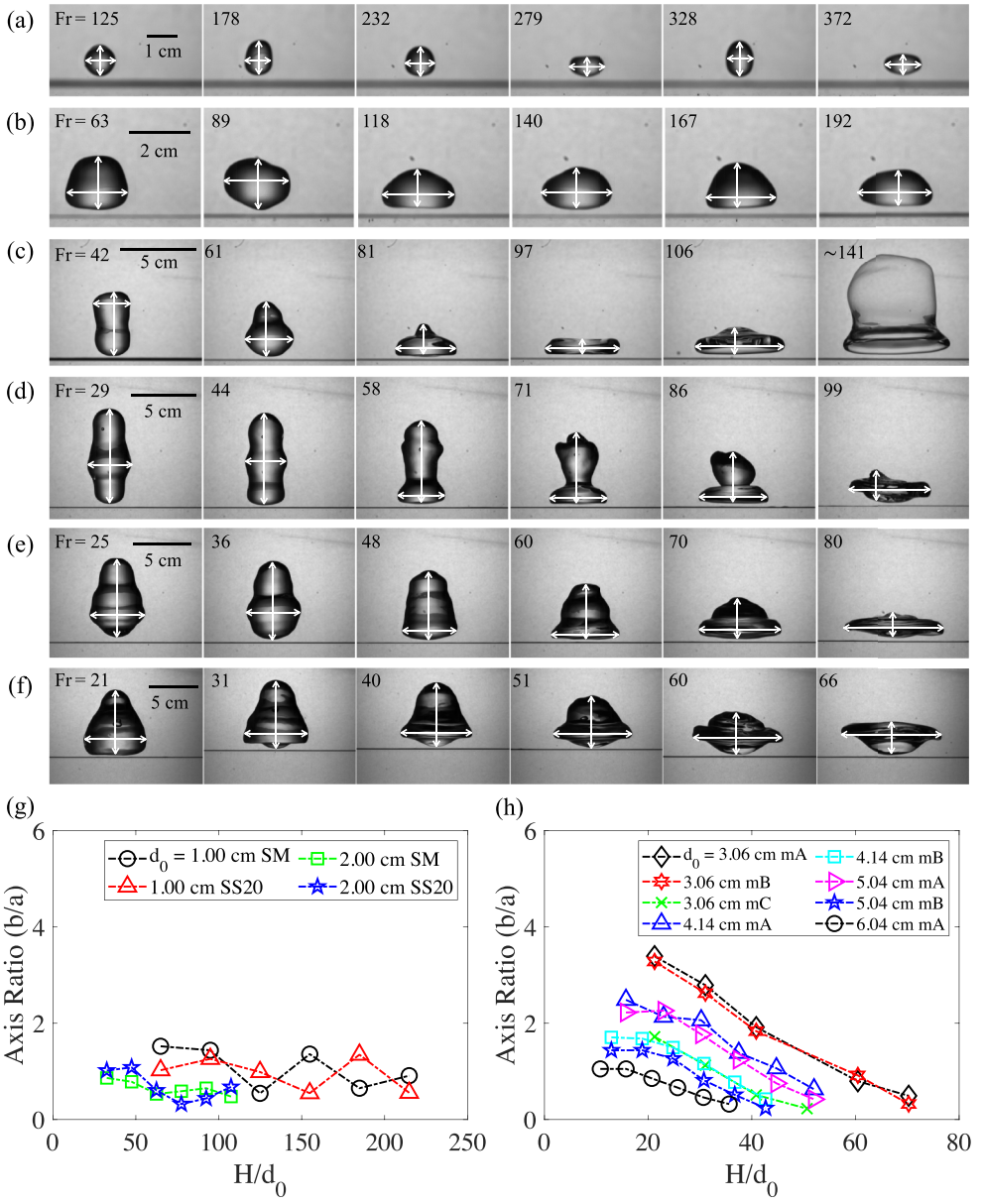

FIG. 6. Droplet shapes just before impact for different liquid volumes and release heights indicated by Froude number: (a) 1.00 cm SS20, (b) 2.00 cm SM, (c) 3.06 cm mC, (d) 4.14 cm mesh B, (e) 5.04 cm mesh B, and (f) 6.04 cm mA. Measurements of a and b are indicated by thin white lines. Case (c) $Fr = 141$ is not included in the rest of the data but is shown for reference. Each row has the same volume and uses the same scale bar. Variation in the droplet axis ratio just before the impact for different nondimensional heights: droplet oscillation regime (g) and flattening regime (h).

resolution and 1/7000 sec exposure time using the Photron FASTCAM SA5. Droplet impact velocity (V), axis ratio (b/a), the evolution of the cavity depth (h) and width (D), maximum cavity depth ($h_{\max}$), and the cavity width corresponding to the maximum cavity depth (D_h) were measured by image processing.

Droplets are formed first by placing a volume from Table I into an appropriate basket that is mounted to the release mechanism at the top of Fig. 4. The release mechanism is connected on one side to a hinge and a solenoid on the other. When the solenoid is released the whole mechanism rotates around the hinge. Since the center of mass is closer to the hinge than the basket, the rotational acceleration of the basket is faster than gravity. Several baskets (Fig. 5) are used depending on the droplet size as marked in Table I.

Table I lists all volumes of the water used for forming large droplets and the corresponding equivalent spherical droplet diameters with names of various surface geometries for releasing the droplet. Actual photographs of the various release geometries used are shown in Fig. 5. The zoomed images of the mesh structures are also shown in Fig. 5. The shape and the net type of mesh A (mA) and mesh B (mB) are similar to the strainer meshes used in kitchen sinks and are hemispherical. Mesh C (mC), sink mesh (SM), and SS20 are specially designed release geometries (more details of these meshes can be found in the work of Fonnesbeck [12]).

TABLE I. Droplet volumes, equivalent diameters, Froude numbers, and droplet release geometries used in the present study.

Volume $\forall_d$(ml)	Equivalent diameter d_0(cm)	Fr	Release geometry
0.525	1.00	123–385	SM, SS20
4.200	2.00	52–192	SM, SS20
15.0	3.06	40–134	mA, mB, mC
37.0	4.14	29–100	mA, mB
67.0	5.04	24–121	mA, mB
115.0	6.04	20–66	mA

All the meshes were coated with the superhydrophobic coating (Glaco Mirror) having a contact angle greater than 160°. Figures 6(a)–6(f) show various droplet shapes at impact and the variation in the droplet axis ratio for oscillating and flattening droplets for different heights in Figs. 6(g) and 6(h), respectively.

APPENDIX B: SMALL AND LARGE DROPLET OSCILLATION FREQUENCY

Figure 7 [12] shows the comparison of the measured droplet oscillation frequencies with the predicted fundamental frequencies (2,0 mode) using the Rayleigh *et al.* [13] theory for droplets less than the capillary length as well as droplets up to 2 cm in diameter. The Rayleigh frequency is

$$f_n^2 = \frac{8n(n-1)(n+2)\sigma}{\rho d_{\rm eq}^3}. \tag{B1}$$

Here n is the mode shape, σ is the surface tension, ρ is the density of the water, and $d_{\rm eq} = d_0$ is the spherical equivalent droplet diameter. The schematic of the (2,0) mode is shown as an inset in Fig. 7, blue shows the nondeformed shape of the droplet, and the two-mode shapes of the droplet are shown in red and yellow. We refer the reader to Fonnesbeck's work [12] for other mode-frequency comparisons, where there is good agreement with the predictions of Raleigh.

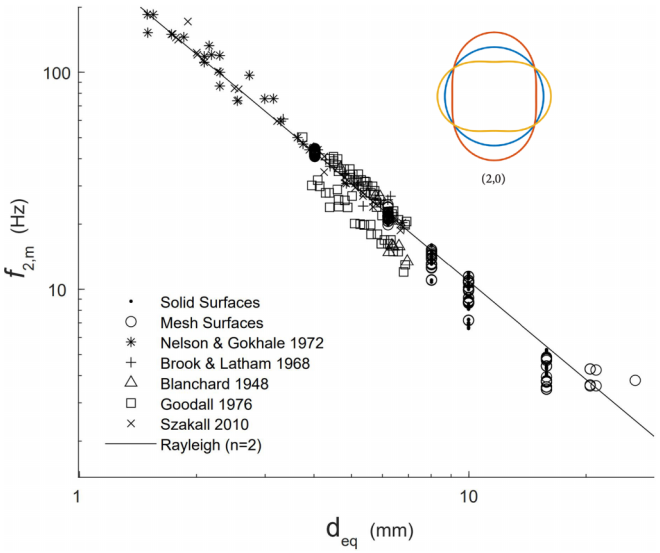

FIG. 7. Measured fundamental frequencies (2,0 mode) of the droplet oscillations for diameters below the capillary length ($\lambda <$ 0.27 cm) up to 2 cm from the work of Fonnesbeck [12]. Inset shows the deformed droplet shapes of mode 2,0.

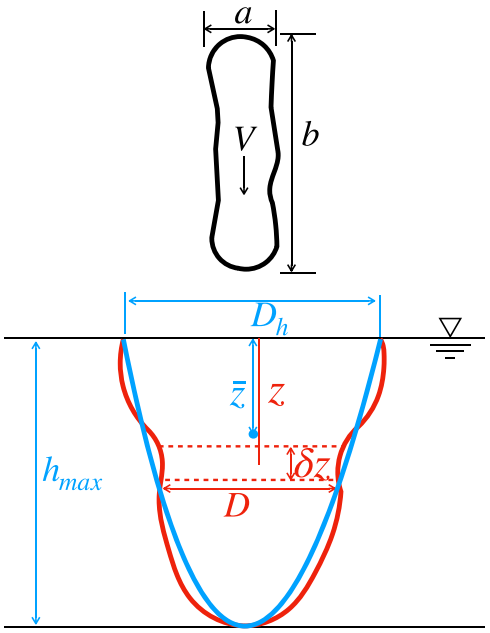

FIG. 8. Schematic of the cavity showing the parameters used for the measurement of the maximum cavity potential energy by (a) ellipsoidal assumption [Eqs. (C2) and (C4)] blue curve and (b) numerical integration [Eq. (C6)] red curve.

APPENDIX C: ENERGY BALANCE

Pumphrey and Elmore [4] obtained the maximum cavity depth by comparing the kinetic energy of the droplet to the potential energy of the cavity. In the present study, we follow a similar approach as in the work of Pumphrey and Elmore [4]; however, we consider the droplet and the cavity shape to be ellipsoidal. The kinetic energy of the impacting droplet is

$$E_{\rm kin} = \tfrac{1}{2}\rho \forall_d V^2. \tag{C1}$$

Let a and b be the horizontal and vertical diameter of the ellipsoidal droplet just before impact (see Fig. 8), then the volume can be formulated as $\forall_d = (\pi a^2 b)/6$. The kinetic energy then becomes

$$E_{\rm kin} = \frac{\rho\pi a^2 b V^2}{12}. \tag{C2}$$

The potential energy of the cavity is easily written as

$$V_{\rm pot} = \frac{\rho\pi D_h^2 h_{\rm max} g\bar{z}}{6}, \tag{C3}$$

where $\bar{z} = \frac{3h_{\rm max}}{8}$ is the distance of the center of mass of the half-ellipsoid from the interface (see Fig. 8). The potential energy of the cavity becomes

$$V_{\rm pot} = \frac{g\rho\pi h_{\rm max}^2 D_h^2}{16}. \tag{C4}$$

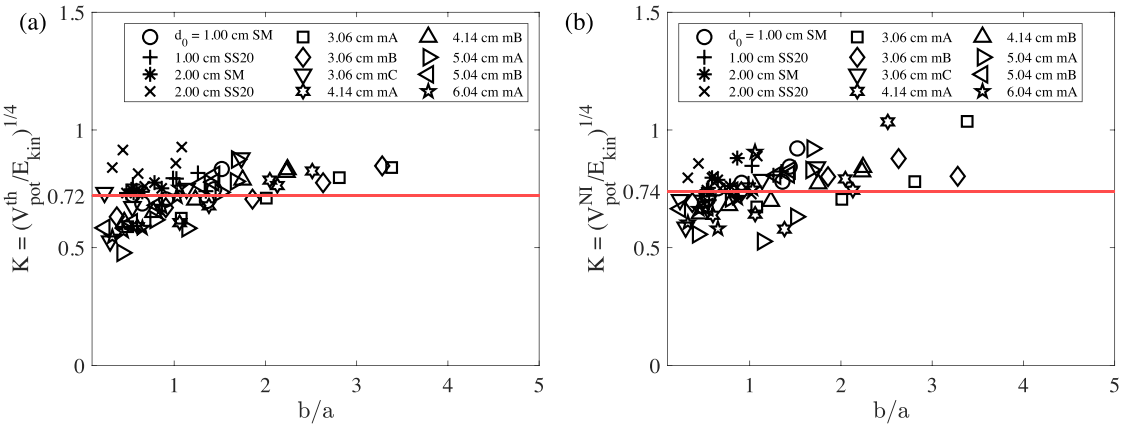

FIG. 9. Droplet kinetic energy at impact and the corresponding maximum potential energy of the cavity. Potential energy is calculated using (a) theory [Eqs. (1) and (2)] and (b) numerical integration of the cavity shape. Least-square fit to the data: (a) $K = 0.72$ for theory and (b) $K = 0.74$ for numerically integrated potential energy.

We can now compare the kinetic energy to the potential energy. Leng [6] showed that only 28% of the kinetic energy is converted into the cavity potential energy for a spherical droplet impact. In the present study, we test this energy argument by considering the energy conversion factor $K = (\frac{V_{\text{pot}}}{E_{\text{kin}}})^{1/4}$ for the nonspherical droplet impacts, and comparing Eqs. (C2) and (C4) we get

$$\frac{h_{\max} D_h}{2ab} = K^2 \left(\frac{V^2}{3gb}\right)^{1/2}. \tag{C5}$$

We can determine the value of K from an ellipsoidal approximation or a numerical integration of the experimental images of the cavity shapes (Fig. 8). The potential energy of the cavity is calculated numerically as

$$V_{\text{pot}}^{NI} = \lim_{\delta z \to 0} \sum^{i} \rho g z_i \frac{\Pi D_i^2}{4} \delta z_i. \tag{C6}$$

We find that the least-square values of the energy conversion factor $K = 0.72$ for the ellipsoidal approximation and 0.74 for the numerically integrated cavities as shown in Fig. 9. These values of K indicate that 29% and 31% of the droplet kinetic energy is getting converted into the cavity potential energy when calculated theoretically and numerically, respectively. Numerically integrated energy does not show much increase in energy conversion, and the difference between the two methods is only 2%; therefore we continue to use the ellipsoidal approximation throughout the paper. Although the droplets are nonspherical the value of $K = 0.72$ obtained by ellipsoidal assumption is very close to the value (0.727) reported for spherical droplet impacts [6]. Hence, we choose the value of $K = 0.72$.

Equation (C5) can now be written as

$$\frac{h_{\max}}{D_h} = 0.72^2 \sqrt{\frac{4V^2 a^3}{3gD_h^4}} \sqrt{\frac{b}{a}}. \tag{C7}$$

Our experimental data show that the value of the term $\sqrt{4V^2a^3/3gD_h^4}$ is a constant [see Fig. 10(a)]. The mean value of this term is $c = 1.12$ when we remove a few of the extreme data points. We justify this removal approximation by noting that it is valid only for cases that obey the relationship $D_h = (4V^2/3gc)^{1/4} a^{3/4}$, which we show in Fig. 10(b). The upper and lower bounds of this behavior show that a few data points fall outside the expected relationship, which can then be removed from the approximation of the mean value in Fig. 10(a), grayed values). The values that fall outside are the largest droplets that have odd shapes [Fig. 6(e) Fr = 80, Fig. 6(f) Fr = 51, Fr = 60, and Fr = 66). We notice that in cases where the bottom most portion of the droplet creates a splash crown or forms a cavity before the maximum a value can impact the cavity. There seems to be a cushioning effect that diminishes the ability a to form a proper value for D_h, thus these extreme cases do not form large enough cavity diameters given their a at impact (see videos 7 and 8 in [1]). Based on these information, the combined value of the constants in Eq. (C7) now become 0.58:

$$\frac{h_{\max}}{D_h} = 0.58 \sqrt{\frac{b}{a}}. \tag{C8}$$

In addition, the value of the constant obtained from the least-square fit to $h_{\max}/D_h$ vs b/a in Fig. 3(e) is also 0.58 independently.

APPENDIX D: A NOTE ON DROPLET SHAPES AT IMPACT

During the cavity retraction of the cases where a jet is formed [Fig. 3(d)], we observe the bubble pinch-off phenomenon similar to the single capillary droplet impacts of Ray *et al.* [32] and Xu *et al.* [33]. In their cases the bubble is formed when the Worthington jet falls back into the bulk fluid. In our cases, the rim portion of the disklike or bagging droplets impacts first on the pool which leads to the generation of an inward crown. The inward motion of the crown merges together at the center of the cavity making an upward jet. Collapsing of the bottom of the cavity onto the inner jet pinches off a large bubble at the cavity bottom during the retraction of the cavity. This phenomenon of the bubble pinch-off is illustrated in video 6 in [1].

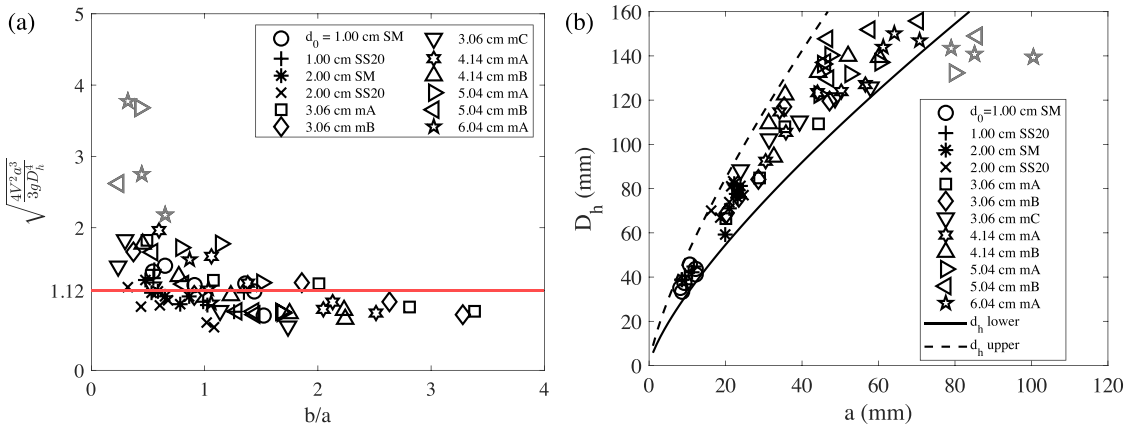

FIG. 10. (a) The constant term for the calculation of the mean value of the constant. (b) Dependence of D_h on a. A few data points fall outside the expected relationship in (b), which are shown in gray, and are not considered for the calculation of the mean value in (a). For the gray points the bottom-most portion of the droplet creates a splash crown or forms a cavity before the maximum a value can impact the cavity. There seems to be a cushioning effect that diminishes the ability for a to form a proper value for D_h.

[1] See Supplemental Material at http://link.aps.org/supplemental/10.1103/PhysRevE.109.045107 for videos 1–8 accompanying this work.

[2] A. M. Worthington, On impact with a liquid surface, Proc. R. Soc. London **34**, 217 (1883).

[3] A. M. Worthington and R. S. Cole, V. Impact with a liquid surface, studied by the aid of instantaneous photography, Philos. Trans. R. Soc. London, Ser. A **189**, 137 (1897).

[4] H. C. Pumphrey and P. A. Elmore, The entrainment of bubbles by drop impacts, J. Fluid Mech. **220**, 539 (1990).

[5] O. G. Engel, Crater depth in fluid impacts, J. Appl. Phys. **37**, 1798 (1966).

[6] L. J. Leng, Splash formation by spherical drops, J. Fluid Mech. **427**, 73 (2001).

[7] A. Bisighini, G. E. Cossali, C. Tropea, and I. V. Roisman, Crater evolution after the impact of a drop onto a semi-infinite liquid target, Phys. Rev. E **82**, 036319 (2010).

[8] U. Jain, M. Jalaal, D. Lohse, and D. van der Meer, Deep pool water-impacts of viscous oil droplets, Soft Matter **15**, 4629 (2019).

[9] J. W. S. B. Rayleigh, *The Theory of Sound*, Vol. 2 (Macmillan & Company, New York, 1896).

[10] A. R. Nelson and N. R. Gokhale, Oscillation frequencies of freely suspended water drops, J. Geophys. Res. **77**, 2724 (1972).

[11] M. Szakáll, S. K. Mitra, K. Diehl, and S. Borrmann, Shapes and oscillations of falling raindrops—A review, Atmos. Res. **97**, 416 (2010).

[12] J. N. Fonnesbeck, Release of large water droplets, Ph.D. thesis, Utah State University, 2022.

[13] J. W. Strutt, VI. On the capillary phenomena of jets, Proc. R. Soc. London **29**, 71 (1879).

[14] N. Rimbert, S. Castrillon Escobar, R. Meignen, M. Hadj-Achour, and M. Gradeck, Spheroidal droplet deformation, oscillation and breakup in uniform outer flow, J. Fluid Mech. **904**, A15 (2020).

[15] E. Villermaux and B. Bossa, Single-drop fragmentation determines size distribution of raindrops, Nat. Phys. **5**, 697 (2009).

[16] D. R. Guildenbecher, C. López-Rivera, and P. E. Sojka, Secondary atomization, Exp. Fluids **46**, 371 (2009).

[17] M. Pilch and C. A. Erdman, Use of breakup time data and velocity history data to predict the maximum size of stable fragments for acceleration-induced breakup of a liquid drop, Int. J. Multiphase Flow **13**, 741 (1987).

[18] G. M. Faeth, L.-P. Hsiang, and P.-K. Wu, Structure and breakup properties of sprays, Int. J. Multiphase Flow **21**, 99 (1995).

[19] A. Wierzba, Deformation and breakup of liquid drops in a gas stream at nearly critical Weber numbers, Exp. Fluids **9**, 59 (1990).

[20] Z. Dai and G. M. Faeth, Temporal properties of secondary drop breakup in the multimode breakup regime, Int. J. Multiphase Flow **27**, 217 (2001).

[21] V. Kulkarni and P. E. Sojka, Bag breakup of low viscosity drops in the presence of a continuous air jet, Phys. Fluids **26**, 072103 (2014).

[22] I. M. Jackiw and N. Ashgriz, On aerodynamic droplet breakup, J. Fluid Mech. **913**, A33 (2021).

[23] J. Han and G. Tryggvason, Secondary breakup of a axisymmetric liquid drops. II. Impulsive acceleration, Phys. Fluids **13**, 1554 (2001).

[24] M. Jain, R. S. Prakash, G. Tomar, and R. V. Ravikrishna, Secondary breakup of a drop at moderate Weber numbers, Proc. R. Soc. London A **471**, 20140930 (2015).

[25] D. T. Ho, C. J. Zappa, W. R. McGillis, L. F. Bliven, B. Ward, J. W. Dacey, P. Schlosser, and M. B. Hendricks, Influence of rain on air-sea gas exchange: Lessons from a model ocean, J. Geophys. Res. [Oceans] **109**, 2003JC001806 (2004).

[26] C. J. Zappa, D. T. Ho, W. R. McGillis, M. L. Banner, J. W. Dacey, L. F. Bliven, B. Ma, and J. Nystuen, Rain-induced turbulence and air-sea gas transfer, J. Geophys. Res. [Oceans] **114**, 2008JC005008 (2009).

[27] T. Frost and R. C. Upstill-Goddard, Air-sea gas exchange into the millennium: Progress and uncertainties, in *Oceanography and Marine Biology, An Annual Review*, Vol. 37 (CRC Press, Boca Raton, 2002), pp. 9–54.

[28] M. Tsimplis and S. A. Thorpe, Wave damping by rain, Nature (London) **342**, 893 (1989).

[29] M. N. Tsimplis, The effect of rain in calming the sea, J. Phys. Oceanogr. **22**, 404 (1992).

[30] D. W. Murphy, C. Li, V. d'Albignac, D. Morra, and J. Katz, Splash behaviour and oily marine aerosol production by raindrops impacting oil slicks, J. Fluid Mech. **780**, 536 (2015).

[31] M. Landeau, R. Deguen, D. Phillips, J. A. Neufeld, V. Lherm, and S. B. Dalziel, Metal-silicate mixing by large earth-forming impacts, Earth Planet. Sci. Lett. **564**, 116888 (2021).

[32] B. Ray, G. Biswas, and A. Sharma, Regimes during liquid drop impact on a liquid pool, J. Fluid Mech. **768**, 492 (2015).

[33] Z. Xu, T. Wang, and Z. Che, Cavity deformation and bubble entrapment during the impact of droplets on a liquid pool, Phys. Rev. E **106**, 055108 (2022).

[34] H. Lhuissier, C. Sun, A. Prosperetti, and D. Lohse, Drop fragmentation at impact onto a bath of an immiscible liquid, Phys. Rev. Lett. **110**, 264503 (2013).

[35] F. Marcotte, G.-J. Michon, T. Séon, and C. Josserand, Ejecta, corolla, and splashes from drop impacts on viscous fluids, Phys. Rev. Lett. **122**, 014501 (2019).

[36] B. D. Fudge, R. Cimpeanu, and A. A. Castrejón-Pita, Dipping into a new pool: The interface dynamics of drops impacting onto a different liquid, Phys. Rev. E **104**, 065102 (2021).

[37] A. A. Castrejón-Pita, J. Castrejón-Pita, and I. M. Hutchings, Experimental observation of von Kármán vortices during drop impact, Phys. Rev. E **86**, 045301(R) (2012).

[38] Z. Jian, M. A. Channa, A. Kherbeche, H. Chizari, S. T. Thoroddsen, and M.-J. Thoraval, To split or not to split: Dynamics of an air disk formed under a drop impacting on a pool, Phys. Rev. Lett. **124**, 184501 (2020).

[39] S. T. Thoroddsen, M.-J. Thoraval, K. Takehara, and T. G. Etoh, Droplet splashing by a slingshot mechanism, Phys. Rev. Lett. **106**, 034501 (2011).

[40] N. B. Speirs, Z. Pan, J. Belden, and T. T. Truscott, The water entry of multi-droplet streams and jets, J. Fluid Mech. **844**, 1084 (2018).

[41] A. Prosperetti and H. N. Oguz, The impact of drops on liquid surfaces and the underwater noise of rain, Annu. Rev. Fluid Mech. **25**, 577 (1993).

[42] A. L. Yarin, Drop impact dynamics: Splashing, spreading, receding, bouncing, Annu. Rev. Fluid Mech. **38**, 159 (2006).

[43] I. Palomba, A. Doria, E. Marconi, M. Bottin, and G. Rosati, Vibration energy harvesting from raindrops impacts: Experimental tests and interpretative models, Appl. Sci. **12**, 3249 (2022).

[44] J. S. Lee, B. M. Weon, S. J. Park, J. T. Kim, J. Pyo, K. Fezzaa, and J. H. Je, Air evolution during drop impact on liquid pool, Sci. Rep. **10**, 5790 (2020).

[45] K. Dhuper, S. D. Guleria, and P. Kumar, Interface dynamics at the impact of a drop onto a deep pool of immiscible liquid, Chem. Eng. Sci. **237**, 116541 (2021).

[46] S. A. Krzeczkowski, Measurement of liquid droplet disintegration mechanisms, Int. J. Multiphase Flow **6**, 227 (1980).